One-Dimensional Nature of Superconductivity at the LaAlO_{3}/SrTiO_{3} Interface

Yun-Yi Pai, Hyungwoo Lee, Jung-Woo Lee, Anil Annadi, Guanglei Cheng, Shicheng Lu, Michelle Tomczyk, Mengchen Huang, Chang-Beom Eom, Patrick Irvin, and Jeremy Levy

Phys. Rev. Lett. **120**, 147001 — Published 6 April 2018

DOI: 10.1103/PhysRevLett.120.147001

One-Dimensional Nature of Superconductivity at the $LaAlO_3/SrTiO_3$ Interface

Yun-Yi Pai,[*,†] *Hyungwoo Lee,*[‡] *Jung-Woo Lee,*[‡] *Anil Annadi, Guanglei Cheng,*[*,†] *Shicheng Lu,*[*,†] *Michelle Tomczyk,*[*,†] *Mengchen Huang,*[*,†] *Chang-Beom Eom,*[‡] *Patrick Irvin,*[*,†] *Jeremy Levy,*[*,†]

[*]Department of Physics and Astronomy, University of Pittsburgh, Pittsburgh, PA 15260, USA

[†]Pittsburgh Quantum Institute, Pittsburgh, PA, 15260 USA

[‡]Department of Materials Science and Engineering, University of Wisconsin-Madison, Madison, WI 53706, USA

We examine superconductivity in $LaAlO_3/SrTiO_3$ channels with widths that transition from the 1D to 2D regime. The superconducting critical current is independent of the channel width and increases approximately linearly with the number of parallel channels. Signatures of electron pairing outside of the superconducting regime are also found to be independent of channel width. Collectively, these results indicate that superconductivity exists at the boundary of these channels and is absent within the interior region of the channels. The intrinsic 1D nature of superconductivity at the $LaAlO_3/SrTiO_3$ interface imposes strong physical constraints on possible electron pairing mechanisms.

Strontium titanate ($SrTiO_3$ or STO) is a superconducting semiconductor [1] whose pairing mechanism has remained unresolved for more than half of a century. Its behavior is similar to that of high-temperature superconductors in many superficial aspects: both exhibit a dome-

shaped superconducting transition temperature versus doping concentration [2], a low-density pseudogap phase [3], a small Fermi energy compared to the Debye frequency [4], and proximity to additional phase transitions [5,6]. A wide range of pairing mechanisms responsible for superconductivity have been considered, including longitudinal optical phonons [7-9], antiferrodistortive modes [10], ferroelectric modes [11], plasmons [12], plasmons with optical phonons [13], and Jahn-Teller bipolarons [14].

Recently, interest in the superconducting properties of STO was revived by the development of STO-based heterostructures and nanostructures, and with the $LaAlO_3/SrTiO_3$ (LAO/STO) system [15] in particular. The two-dimensional interface supports superconductivity [16], and it can be electrostatically gated to trace out a superconducting dome [17], similar to the dome originally obtained through chemical doping [2]. The heterostructure geometry has enabled new probes of the superconducting state that were not feasible previously. For example, planar tunneling experiments have revealed evidence for a pseudogap phase [3] with unexpected in-gap states [18]. Scanning SQUID images [19] show signatures of strong inhomogeneities in superfluid density linked to naturally forming ferroelastic domain structures. Mesoscopic devices created within the LAO/STO interface reveal multiple gap features that have been interpreted as signatures of spin-triplet pairing [20].

Further reduction in dimensionality of LAO/STO devices has become possible through the use of various lithographic techniques [21-25]. Here we use conductive-atomic force microscope (c-AFM) lithography [26,27], which relies on AFM tip-controlled protonation/deprotonation [28,29] of the LAO surface. A variety of quasi-1D and confined ("quasi-0D") structures have been created, including superconducting nanowires [30], ballistic 1D channels [31], and single-electron transistors [32], that revealed the existence of electron

pairing outside the superconducting state [33]. Despite all of the new information about the superconducting phase, the microscopic origin of the pairing "glue" remains a mystery.

Here, we systematically investigate low-temperature transport behavior in conducting channels, formed at the LAO/STO interface using c-AFM lithography, with widths ranging between 10 nm and 1 μm. LAO/STO heterostructures are grown by pulsed laser deposition with growth parameters reported in Ref. [29]. The thickness of LAO is fixed to 3.4 u.c. (defined by the number of Reflection High-Energy Electron Diffraction oscillations), resulting in an interface that is close to the critical thickness for the metal-insulator transition [34]. Electrical contact to the LAO/STO interface is made by Ar^+ etching (25 nm) followed by sputter depositing Ti/Au (4 nm/25 nm). Conductive nanostructures at the LAO/STO interface are subsequently created using c-AFM lithography [26].

The first family of devices considered here (FIG. 1(a)) consists of three sections in series with characteristic widths $w_1 \sim 10$ nm, $w_2 = 100$ nm, and $w_3 = 1$ μm. All three sections (which are subsequently referred to as w_1, w_2, and w_3 sections) have the same length $L = 3$ μm. The w_1 section is created by writing a single line, while sections w_2 and w_3 are created by raster-scanning a rectangular area along the two principal axes. Conductive rectangular shapes separate the individual wire segments, enabling each to be monitored simultaneously and independently.

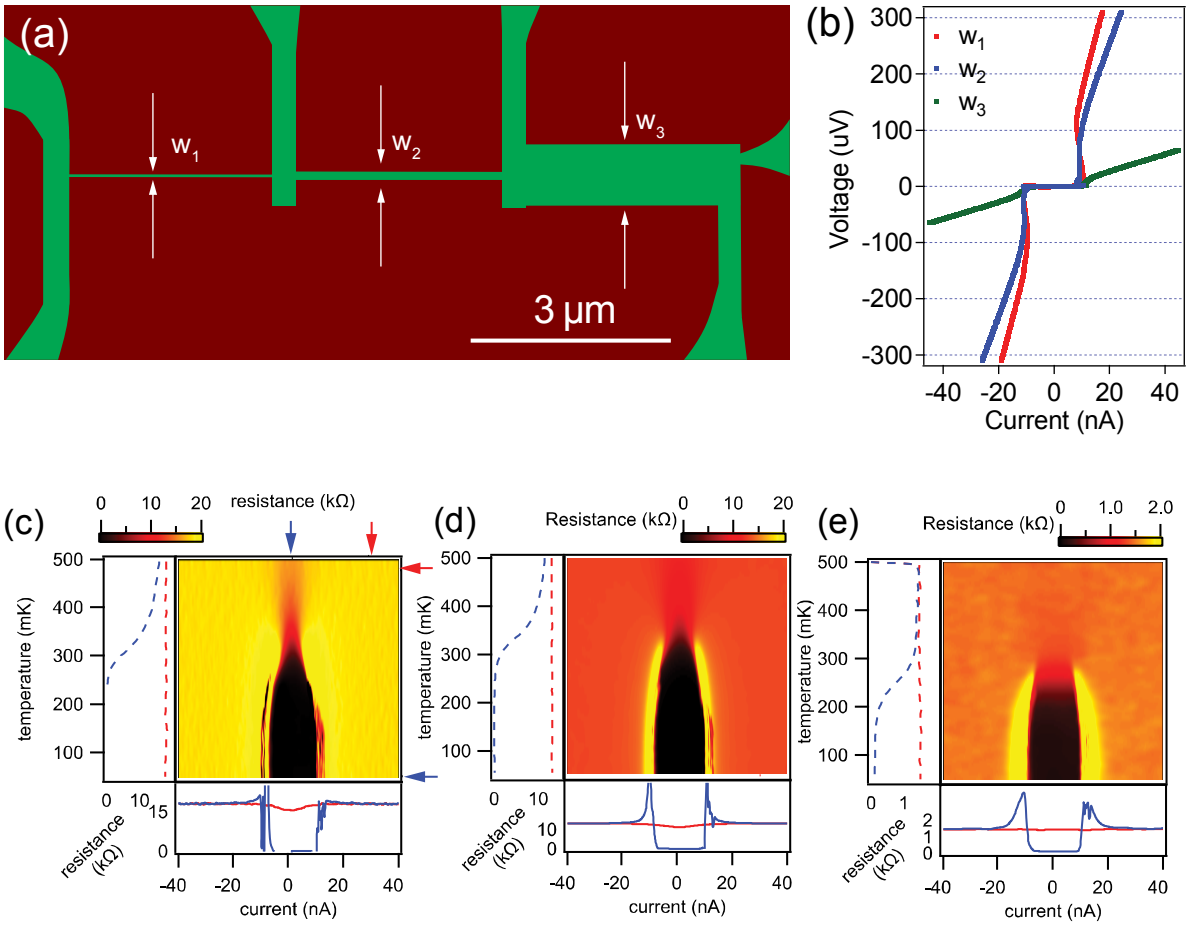

FIG. 1. (a) LAO/STO device (top view) consisting of three sections with widths $\boldsymbol{w_1 = 10\ nm}$, $\boldsymbol{w_2 = 100\ nm}$, and $\boldsymbol{w_3 = 1000\ nm}$. All three sections have the same length $\boldsymbol{L = 3\ \mu m}$. Green (red) areas depict conducting (insulating) regions (b) *I-V* curves for different channels measured at 50 mK and V_{bg} = -6.5 V. (c-e) Differential resistance (dV/dI) as a function of current and temperature. (c) w_1 section, (d) w_2 section, and (e) w_3 section. Data taken at V_{bg} = -6.5 V and B = 0 T.

After c-AFM lithography, the devices are transferred into a dilution refrigerator and cooled to $T = 50$ mK. Four-terminal current-voltage (*I-V*) measurements for each of the three sections are recorded as a function of out-of-plane magnetic field (B), temperature, and back-gate voltage (V_{bg}) which tunes the carrier density [17]. We identify the sharp increase in differential resistance above a critical value I_c with the superconducting switching current, which provides a lower bound for the actual critical current due to various phase-slip mechanisms [35]. The results reported here are representative of three nominally identical sets of devices that show qualitatively similar behavior. FIG. 1(b) shows the 4-terminal *I-V* curves for the three sections at

a back-gate voltage of $V_g = -6.5$ V and $T = 50$ mK. While all three sections are superconducting, the critical current $I_{c,i}$ (where i=1,2,3 is the channel index) within each section is remarkably similar (~10 nA), i.e., *independent of the channel width*. By contrast, the normal-state resistance (*i.e.*, resistance under dc bias that exceeds $I_{c,i}$) decreases monotonically with increasing width: R_1=17 kΩ for w_1, R_2=11.5 kΩ for w_2, and R_3=1.4 KΩ for w_3. In particular, the ratio of the normal state resistance of section w_2 and section w_3 is nearly equal to the ratio of the widths w_2/w_3, indicating that the 1D-2D crossover takes place near 100 nm, and that electric flux-focusing effects are not strongly affecting the transverse carrier density profiles in the 2D regime.

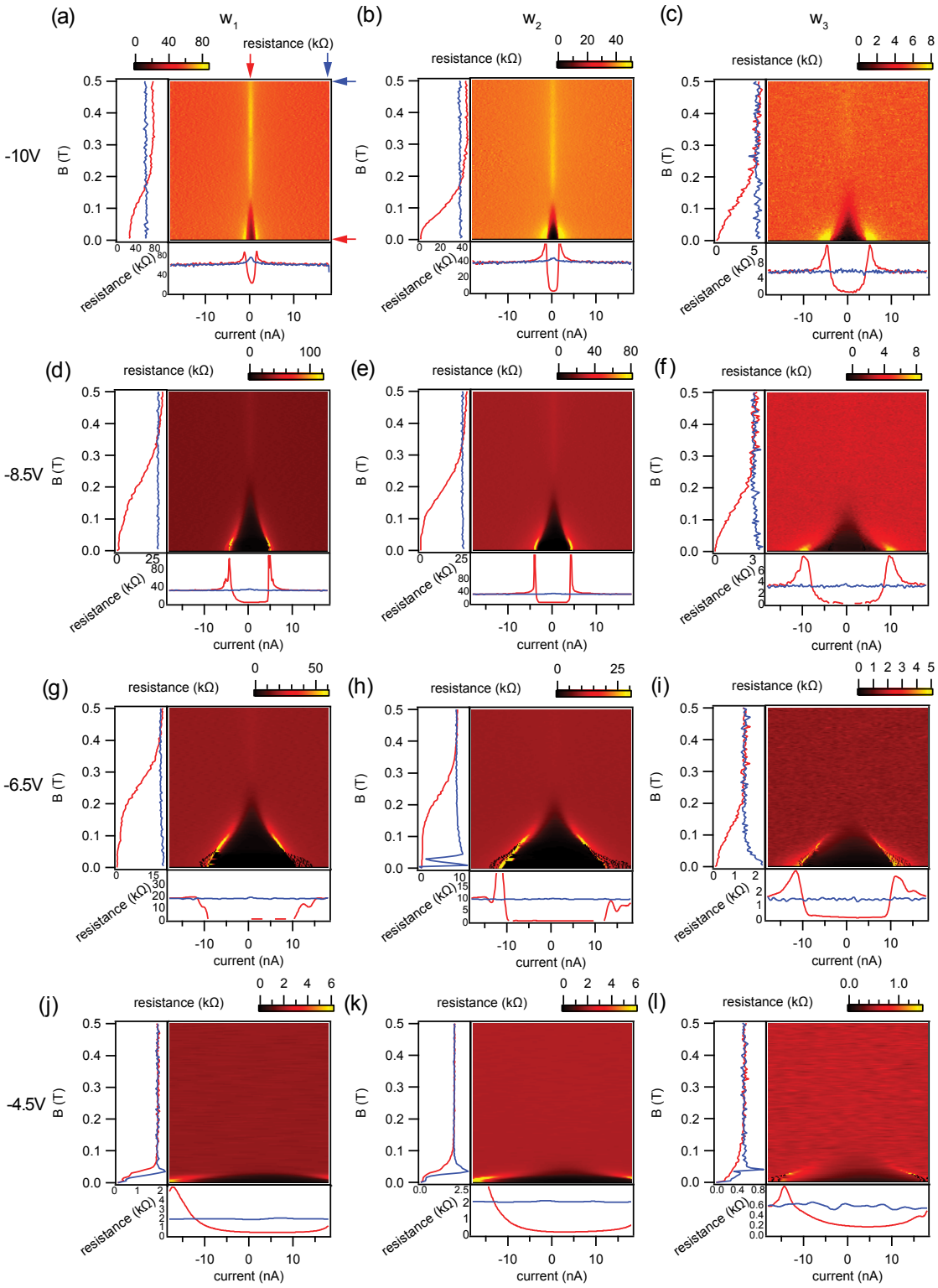

FIG. 2. Differential resistance (dV/dI), plotted as a function of current and magnetic field, for each of the three sections at different backgate voltages. The lower panel for each graph shows the horizontal linecuts at B = 0 T (red) and B = 0.5 T (blue). The left panel shows the vertical linecuts at bias current I_1 = 0 nA (red) and I_2 =14.5 nA (blue).

Further insight into the superconducting nature of these channels comes from examining the differential resistance (dV/dI), obtained from numerical differentiation of the I-V curves. FIG. 1(c-e) shows the differential resistance of the three different sections as a function of current and temperature. Linecuts at fixed temperatures ($T_1 = 50$ mK, $T_2 = 475$ mK) and bias currents ($I_1 = 0$ nA,$I_2 = 30$ nA), indicated by arrows, are shown for each device. The superconducting transition temperature is about $T_c \sim 300$ mK for sections w_1 and w_2, and slightly lower ($T_c \sim 250$ mK) for section w_3. Notably, when $T > T_c$ a zero bias conductance peak (dip in the differential resistance dV/dI) is observed, for both w_1 and w_2 sections (FIG. 1(c,d)). This feature is much less pronounced for the widest section, w_3 (FIG. 1(e)).

FIG. 2 tracks the differential resistance of the three sections as a function of bias current, magnetic field and gate voltage. Intensity plots of $dV/dI(B, I)$ are shown for selected values of V_{bg}. A number of observations can be made:

(i) The superconducting upper critical field $\mu_0 H_{c2}$ initially increases with increasing backgate and then decreases. This non-monotonic dependence is reminiscent of the superconducting dome commonly observed for this interface [17].

(ii) The critical current increases monotonically when increasing the backgate voltages for all three sections. The critical currents for the three sections are strikingly similar to one another, except at the most negative backgate value.

(iii) A zero-bias conductance dip (peak in the differential resistance dV/dI) is observed above H_{c2} (e.g., FIG. 2 (a)) and is most pronounced at the most negative backgate voltages. We associate this feature, as well as the zero-bias conductance peak in FIG. 1 (c-e), with a previously identified phase in which electrons are paired but

not superconducting [33]. FIG. 3 shows the cross sections of the zero-bias conductance dip for the three sections. The conductance dip for the three section widths (FIG. 3) is nearly the same for the w_1 and w_2 sections, and it is approximately twice as large for the w_3 channel. The conductance dip therefore appears to behave similarly to the superconducting critical current, in that it does not increase linearly with the channel width.

(iv) The pronounced differences between the widest section, w_3, and the two narrower sections cannot be ascribed to the writing process, since section w_2 is created by raster-scanning and w_1 is created by moving the AFM tip along a single line. In other words, the fact that sections w_1 and w_2 behave similarly, and significantly different from section w_3, illustrates that the pairing is influenced by the physical geometry rather than the method in which the conducting regions are produced.

The results presented thus far are consistent with a scenario in which superconductivity and pairing exist within a quasi-1D (w~50-100 nm) portion of the channel, and in which superconductivity and pairing coexist with a parallel, non-superconducting (2D) bulk phase. The superconducting critical current density for section w_3 ($j_C \sim 10\ \mathrm{nA/\mu m}$) is comparable to what has been reported for the bulk LAO/STO interface [16,36], while the critical current density of section w_2 is an order of magnitude higher.

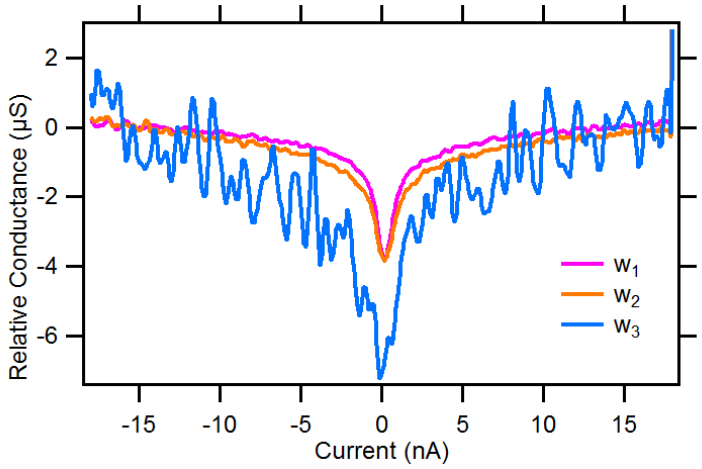

FIG. 3. The zero-bias conductance dip for the three sections. The curves are a result of averaging over the range of magnetic field values B = 0.23 T—0.73 T, at backgate V_{bg} = -10 V. Note that the size of the zero-bias conductance dip is similar for sections w_1 and w_2, and approximately twice as large for section w_3.

A possible explanation is that superconductivity exists only within a 1D region of the 2D channel, i.e., the outer edge(s). To test the hypothesis, we investigate a second type of device, as shown in FIG. 4(a). The device consists of three sections in series: from left, a single $w_1 \sim 10$ nm nanowire ("w_1"), a section of five parallel nanowires of width 10 nm ("$5w_1$") spaced 200 nm apart, and a $w_3 = 1$ μm section ("w_3"). The differential resistance dV/dI (I, V_{sg}) is measured for each of the three sections (FIG. 4 (b-d)). Overall, the conductance of this device is higher, reflecting the available range over which this device could be gated. At gate voltages $V_{bg} < -20\ V$, the voltage leads become insulating, preventing reliable measurements from being made. The critical current for the $5w_1$ channel is 4-5 times larger than the other two sections, and it exhibits a different dependence on back-gate voltage. Meanwhile, channels w_1 and w_3 have similar superconducting critical currents; however, w_3 possesses a non-superconducting, parallel conductance that is an order-of-magnitude larger than channel w_1. This second class of

experiments support the idea that superconductivity is associated with the channel boundaries, and that the interior bulk of the channels do not form a superconducting phase.

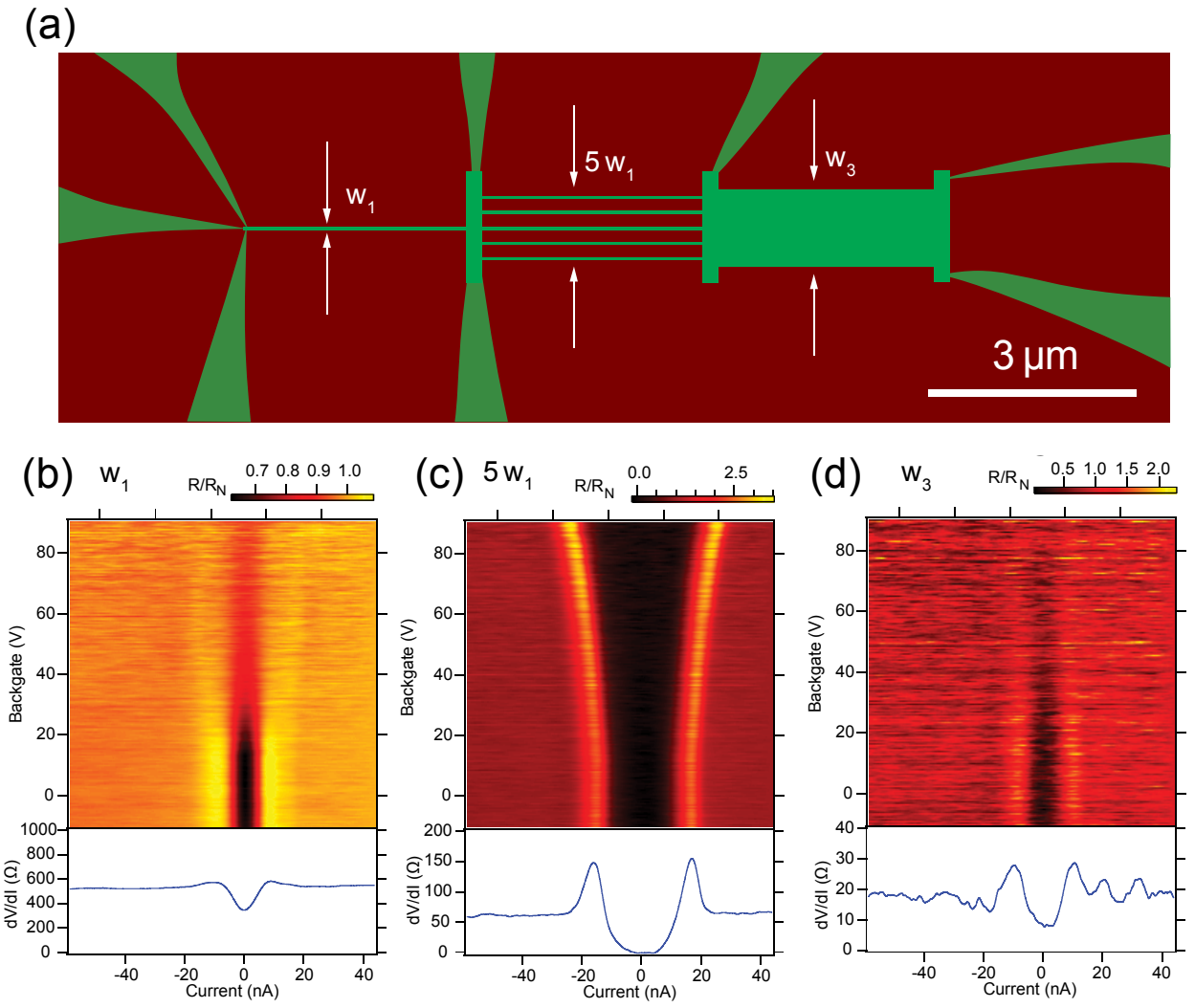

FIG. 4. (a) Multi-channel device consist of three sections. Left: single nanowire (w_1). Middle: five nanowires in parallel, 200 nm apart ($5w_1$). Right: 1 μm-wide channel (w_3). All three sections have the same length L = 3 μm. (b) The normalized differential resistance as a function of current and the backgate voltage, for the single nanowire section. The differential resistance in the color scale is normalized with respect to the normal state value. Lower panel: linecut of the raw differential resistance for the w_1 section, (c) $5w_1$ section, and (d) w_3 section, at backgate V = 0 V. All data shown here is acquired at T= 30 mK.

What might cause only the conducting boundaries of these channels to be superconducting? One possibility is that the center of the conductive channels is overdoped, i.e., on the high-density side of the superconducting dome, while the surrounding area is insulating, i.e., underdoped. In this scenario, a quasi-1D strip for which the doping is optimal should exist along each boundary (FIG. 5(a)). This simple picture satisfactorily predicts a width-independent critical current, and gives the correct scaling of parallel background conductance. However, this scenario does not explain why there should be a superconducting dome in the first place.

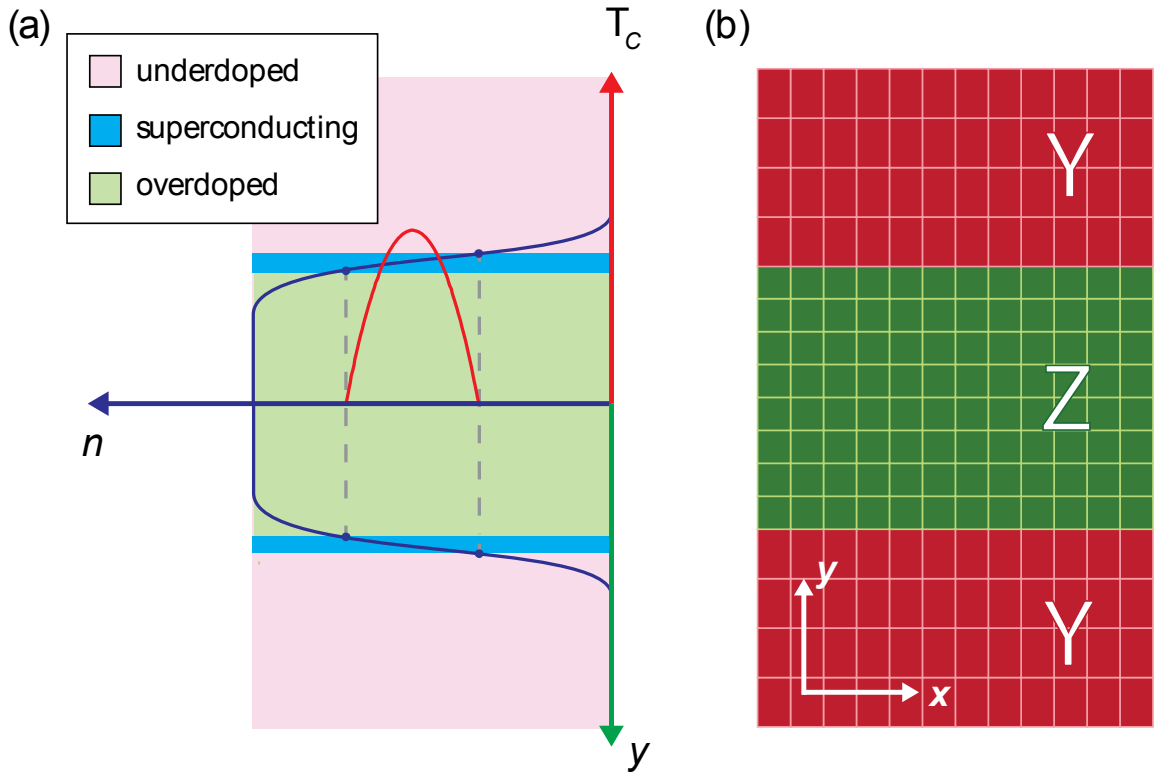

FIG. 5. (a) Schematic illustrating how quasi-1D regions of optimal doping can be found near the insulating boundaries of a 2D conducting channel that is overdoped in the 2D bulk region. Dashed lines indicate lower and upper boundaries of the superconducting dome (red curve). The electron density profile (dark blue curve) is overdoped in the center, underdoped in the insulation regions, and optimally doped along a narrow region on both edges, where the density falls within the superconducting dome. (b) Illustration of expected ferroelastic domain structure associated with a conductive region (Z domain) surrounded by insulating boundaries (Y domains).

STO undergoes a cubic-to-tetragonal antiferrodistortive transition at T_{AFD} = 105 K. The transition combines antiphase rotations of TiO_6 cages with elongation of the unit cell along the axis of the rotation. Below this transition, ferroelastic domains form with different orientations (*X, Y, Z*), separated by nanometer-scale domain walls. These domain walls can be driven by electrostatic gating [37] and are observed to be highly conductive [19]. Previously, piezoelectric force microscopy imaging experiments on conductive LAO/STO nanostructures show that conductive regions formed by c-AFM lithography form regions elongated in z-direction (surrounded by cubic insulating regions) at room temperature [38]. This elongation configuration is expected to persist to low temperatures and seed the formation of the Z-oriented ferroelastic domains surrounded by regions that have strain-compensating *X* or *Y* domains (FIG. 5(b)). Ferroelastic domain boundaries created at room temperature by c-AFM lithography thus naturally coincide with the edges that separate conducting and insulating regions.

If ferroelastic domain walls indeed bracket the edges of conducting nanostructures, one may naturally wonder whether they can mediate electron pairing. Ferroelastic domain walls, with widths that are believed to be comparable to the unit cell [39], possess structural, electronic, and point-defect properties that differ significantly from the uniform domains, which can vary from ~10 nanometers to many micrometers in extent. Typical superconducting critical current densities reported for 2D LAO/STO are consistent with an average density of one domain wall per micron, where each domain wall is associated with ~10 nA of supercurrent. The domain walls position may fluctuate dynamically and couple to electronic states, yielding an attractive interaction. Alternatively, ferroelastic domain walls may trap high densities of oxygen vacancies [40] or other point defects that act as negative-U centers [41,42]. Far outside of the superconducting regime (either $T > T_c$ or $|B| > \mu_0 H_{c2}$), signatures of pairing without

superconductivity [33] are observed that scale independently of the width of the channel. In Fig. 1(c,d), a zero-bias conductance dip appears for temperatures as high as $T = 500$ mK, while are zero-bias resistive features persist at high magnetic fields that are similar in nature to pseudogap signatures reported by Richter et al. [3] and multigap features measured by Stornaiuolo et al. [20].

The presence and relevance of quasi-1D channels is not restricted to the artificially constructed channels created by c-AFM lithography. A variety of spatially-resolved imaging techniques have revealed strongly inhomogeneous electron transport at the 2D LAO/STO interface, and have demonstrated that current flows preferentially along ferroelastic domain boundaries, affecting properties in both the normal state [19,43,44] and superconducting [45] regime.

Regardless of the pairing mechanism, superconductivity in the strict 1D limit is of fundamental interest of its own right [35,46]. Low-dimensional superconductivity has been considered in several proposals to support Majorana fermions [47,48]. While there are theoretical predictions for topologically protected edge modes at STO surfaces [49], there is no evidence so far that topology plays an important role in stabilizing the superconducting state in the LAO/STO structures described here.

In conclusion, we have presented evidence that superconductivity at the LAO/STO interface naturally exists within quasi-1D channels at the edge of conducting 2D regions. The conclusion is supported by transport measurements for two families of devices in which the size and number of nanoscale channels is systematically varied. While the microscopic mechanism for electron pairing and superconductivity in STO is still unresolved, the experimental results

presented here provide new stringent geometric constraints and suggest a possible role played by ferroelastic domain boundaries.

AUTHOR INFORMATION

Corresponding Author

*E-mail: jlevy@pitt.edu

NOTES

The authors declare no competing financial interest.

ACKNOWLEDGMENTS

We acknowledge helpful discussions with David Pekker, Yuhe Tang, and Anthony Tylan-Tyler. J.L. acknowledges support from the Vannevar Bush Faculty Fellowship program sponsored by the Basic Research Office of the Assistant Secretary of Defense for Research and Engineering and funded by the Office of Naval Research (N00014-15-1-2847).

REFERENCES

[1] J. F. Schooley, W. R. Hosler, and M. L. Cohen, Phys Rev Lett **12**, 474 (1964).
[2] C. S. Koonce, M. L. Cohen, J. F. Schooley, W. R. Hosler, and E. R. Pfeiffer, Phys Rev **163**, 380 (1967).
[3] C. Richter *et al.*, Nature **502**, 528 (2013).
[4] C. Lin and A. A. Demkov, Phys Rev Lett **111**, 217601 (2013).
[5] S. E. Rowley, L. J. Spalek, R. P. Smith, M. P. M. Dean, M. Itoh, J. F. Scott, G. G. Lonzarich, and S. S. Saxena, Nat Phys **10**, 367 (2014).
[6] C. W. Rischau *et al.*, Nat Phys **13**, 643 (2017).
[7] M. L. Cohen, Reviews of Modern Physics **36**, 240 (1964).
[8] A. Baratoff and G. Binnig, Physica B+C **108**, 1335 (1981).
[9] L. P. Gor'kov, Proceedings of the National Academy of Sciences **113**, 4646 (2016).
[10] J. Appel, Phys Rev **180**, 508 (1969).
[11] J. M. Edge, Y. Kedem, U. Aschauer, N. A. Spaldin, and A. V. Balatsky, Phys Rev Lett **115**, 247002 (2015).
[12] J. Ruhman and P. A. Lee, Phys Rev B **94**, 224515 (2016).
[13] Y. Takada, Journal of the Physical Society of Japan **49**, 1267 (1980).
[14] A. Stashans, H. Pinto, and P. Sanchez, J Low Temp Phys **130**, 415 (2003).

[15] A. Ohtomo and H. Y. Hwang, Nature **427**, 423 (2004).
[16] N. Reyren *et al.*, Science **317**, 1196 (2007).
[17] A. D. Caviglia *et al.*, Nature **456**, 624 (2008).
[18] L. Kuerten, C. Richter, N. Mohanta, T. Kopp, A. Kampf, J. Mannhart, and H. Boschker, Phys Rev B **96**, 014513 (2017).
[19] B. Kalisky *et al.*, Nature Materials **12**, 1091 (2013).
[20] D. Stornaiuolo, D. Massarotti, R. Di Capua, P. Lucignano, G. P. Pepe, M. Salluzzo, and F. Tafuri, Phys Rev B **95**, 140502 (2017).
[21] A. Ron and Y. Dagan, Phys Rev Lett **112**, 136801 (2014).
[22] P. P. Aurino, A. Kalabukhov, N. Tuzla, E. Olsson, T. Claeson, and D. Winkler, Applied Physics Letters **102**, 201610 (2013).
[23] C. W. Schneider, S. Thiel, G. Hammerl, C. Richter, and J. Mannhart, Applied Physics Letters **89**, 122101 (2006).
[24] A. Ron, E. Maniv, D. Graf, J. H. Park, and Y. Dagan, Phys Rev Lett **113**, 216801 (2014).
[25] A. M. R. V. L. Monteiro, D. J. Groenendijk, N. Manca, E. Mulazimoglu, S. Goswami, Y. Blanter, L. M. K. Vandersypen, and A. D. Caviglia, Nano Lett (2017).
[26] C. Cen, S. Thiel, G. Hammerl, C. W. Schneider, K. E. Andersen, C. S. Hellberg, J. Mannhart, and J. Levy, Nature Materials **7**, 298, 10.1038/nmat2136 (2008).
[27] C. Cen, S. Thiel, J. Mannhart, and J. Levy, Science **323**, 1026 (2009).
[28] F. Bi, D. F. Bogorin, C. Cen, C. W. Bark, J. W. Park, C. B. Eom, and J. Levy, Applied Physics Letters **97**, 173110 (2010).
[29] K. A. Brown *et al.*, Nature Communications **7**, 10681 (2016).
[30] J. P. Veazey *et al.*, Nanotechnology **24**, 375201 (2013).
[31] M. Tomczyk *et al.*, Phys Rev Lett **117**, 096801 (2016).
[32] G. Cheng *et al.*, Nat Nanotechnol **6**, 343 (2011).
[33] G. Cheng *et al.*, Nature **521**, 196 (2015).
[34] S. Thiel, G. Hammerl, A. Schmehl, C. W. Schneider, and J. Mannhart, Science **313**, 1942 (2006).
[35] F. Altomare and A. M. Chang, *One-Dimensional Superconductivity in Nanowires* (Wiley, 2013).
[36] S. Hurand *et al.*, Scientific Reports **5**, 12751 (2015).
[37] M. Honig, J. A. Sulpizio, J. Drori, A. Joshua, E. Zeldov, and S. Ilani, Nature Materials **12**, 1112 (2013).
[38] M. Huang, F. Bi, S. Ryu, C.-B. Eom, P. Irvin, and J. Levy, APL Materials **1**, 052110 (2013).
[39] G. Catalan, J. Seidel, R. Ramesh, and J. F. Scott, Reviews of Modern Physics **84**, 119 (2012).
[40] L. Goncalves-Ferreira, S. A. T. Redfern, E. Artacho, E. Salje, and W. T. Lee, Phys Rev B **81**, 024109 (2010).
[41] P. W. Anderson, Phys Rev Lett **34**, 953 (1975).
[42] Y. Matsushita, H. Bluhm, T. H. Geballe, and I. R. Fisher, Phys Rev Lett **94**, 157002 (2005).
[43] Y. Frenkel, N. Haham, Y. Shperber, C. Bell, Y. Xie, Z. Chen, Y. Hikita, H. Y. Hwang, and B. Kalisky, ACS Applied Materials & Interfaces **8**, 12514 (2016).
[44] N. J. Goble, R. Akrobetu, H. Zaid, S. Sucharitakul, M.-H. Berger, A. Sehirlioglu, and X. P. A. Gao, Scientific Reports **7**, 44361 (2017).

[45] H. Noad *et al.*, Phys Rev B **94**, 174516 (2016).
[46] A. Bezryadin, *Superconductivity in Nanowires: Fabrication and Quantum Transport* (Wiley, 2013).
[47] Y. Oreg, G. Refael, and F. von Oppen, Phys Rev Lett **105**, 177002 (2010).
[48] R. M. Lutchyn, J. D. Sau, and S. Das Sarma, Phys Rev Lett **105**, 077001 (2010).
[49] M. Vivek, M. O. Goerbig, and M. Gabay, Phys Rev B **95**, 165117 (2017).